Key Points:
- Magma storage conditions from H_2O and CO_2 measurements of melt inclusions are integrated with recent geophysical observations
- Mafic recharge promotes rhyolitic volcanism by flushing the reservoir with volatiles and promoting accumulation of exsolved fluids
- Volatile-rich melt inclusions record decompression, fractional crystallization, and evolution of rhyolite between depths of ~14 and 4 km

Storage and Evolution of Laguna del Maule Rhyolites: Insight From Volatile and Trace Element Contents in Melt Inclusions

Jacob D. Klug[1] [ID]**, Brad S. Singer[1]** [ID]**, Noriko T. Kita[1], and Michael J. Spicuzza[1]**

[1]Department of Geoscience, University of Wisconsin-Madison, Madison, WI, USA

Abstract Interpreting unrest at silicic volcanoes requires knowledge of the magma storage conditions and dynamics that precede eruptions. The Laguna del Maule volcanic field, Chile, has erupted ~40 km³ of rhyolite over the last 20 ka. Astonishing rates of sustained surface inflation at >25 cm/year for >12 years reveal a large, restless system. Integration of geochronologic, petrologic, geomorphic, and geophysical observations provides an unusually rich context to interpret ongoing and prehistoric processes. We present new volatile (H_2O, CO_2, S, F, and Cl), trace element, and major element concentrations from 109 melt inclusions hosted in quartz, plagioclase, and olivine from seven eruptions. Silicic melts contain up to 8.0 wt. % H_2O and 570 ppm CO_2. In rhyolites melt inclusions track decompression-driven fractional crystallization as magma ascended from ~14 to 4 km. This mirrors teleseismic tomography and magnetotelluric findings that reveal a domain containing partial melt spanning from 14 to 4 km. Ce and Cl contents of rhyolites support the generation of compositionally distinct domains of eruptible rhyolite within the larger reservoir. Heat, volatiles, and melt derived from episodic mafic recharge likely incubate and grow the shallow reservoir. Olivine-hosted melt inclusions in mafic tephra contain up to 2.5 wt. % H_2O and 1,140 ppm CO_2 and proxy for the volatile load delivered via recharge into the base of the silicic mush at ~14 to 8 km. We propose that mafic recharge flushes deeper reaches of the magma reservoir with CO_2 that propels H_2O exsolution, upward accumulation of fluid, pressurization, and triggering of rhyolitic eruptions.

1. Introduction

Tephra and lava from recently active silicic magmatic systems hold many clues to the storage conditions and processes that cause unrest, which may manifest as surface deformation, seismicity, or gas emissions that precede eruptions (e.g., Biggs & Pritchard, 2017; Singer, Jicha, et al., 2014). Multiple lines of petrologic evidence suggest that large silicic systems persist in the shallow crust as mostly crystalline "mush" reservoirs with small fractions of interstitial melt that may be extracted to form crystal-poor bodies of eruptible rhyolite (Andersen et al., 2019; Bachmann & Bergantz, 2004; Hildreth, 2004). Diffusion chronometry suggests that relatively cool, long-lived reservoirs may be destabilized rapidly by mafic recharge to produce rhyolitic eruptions on time scales of only months to centuries (Andersen et al., 2017, 2018; Druitt et al., 2012; Singer et al., 2016; Till et al., 2015; Wark et al., 2007). How these magma reservoirs are incubated over thousands of years and grow to large volumes in the shallow crust, and whether magma injection or fluid pressurization are responsible for destabilization, unrest, and eruption, is a topic of great interest (e.g., Andersen et al., 2017; Barboni et al., 2016; Gelman et al., 2013; Huber et al., 2019; Jackson et al., 2018; Pritchard et al., 2019; Reath et al., 2020; Rubin et al., 2017; Till et al., 2015). A case has been made for a deep origin of rhyolite by Annen et al. (2006); however, another explanation is that the addition of relatively hot, recharge magma to the base of crystal-rich mush stored in the upper crust incubates and provides heat to aid in melting of cumulate and crustal rocks and provides volatiles that promote the extraction of rhyolite in the shallow crust (Bachmann & Bergantz, 2004; Druitt et al., 2012; Hildreth, 2004; Singer et al., 2016; Wark et al., 2007). Moreover, contrasts in the major and trace element compositions of crystals and their temperature of formation within a single magmatic system are interpreted to reflect thermal heterogeneity and co-existence of discrete small volume melt-rich domains within larger, mostly crystalline reservoirs (Andersen et al., 2019; Rubin et al., 2017).

Figure 1. Regional map of the Southern Volcanic Zone (SVZ), with Laguna del Maule's (LdM) location shown as a red star (modified from Andersen et al., 2017). Other selected volcanoes are shown with white triangles. The inset diagram shows the position of LdM in the greater geographic context of South America.

Volatiles, including H_2O and CO_2, also play a fundamental role in the evolution and eruption of silicic (>65 wt. % SiO_2) magma systems (Caricchi et al., 2018; Degruyter et al., 2017; Huber & Parmigiani, 2018; Parmigiani et al., 2016). Both the initial H_2O and CO_2 dissolved in the melt and as an exsolved fluid phase are important, as they may (1) reflect the transfer of H_2O and CO_2 from recharge magma into silicic magma (Andersen et al., 2018; Bachmann & Bergantz, 2006; Caricchi et al., 2018; Degruyter et al., 2017; Huber et al., 2011), (2) promote melt migration through silicic crystal mushes (Hartung et al., 2019; Huber & Parmigiani, 2018; Parmigiani et al., 2016), and (3) propel second boiling, inflation of magma reservoirs, surface deformation, and explosive behavior (Blundy & Cashman, 2008; Degruyter et al., 2017). Moreover, crustal rheology and the abundance of exsolved volatiles may be the key controls on eruption size and whether or not a shallow magma reservoir can grow for a protracted period (Huber et al., 2019). Huber et al. (2019) demonstrate that when recharge flux is enhanced, large long-lived and eruptible magma reservoirs commonly grow at pressures between 1.5 and 2.5 kbar (6 to 8 km depth), with deeper, non-eruptible, plutonic roots evolving at pressures >2.5 kbar. A complicating factor in determining pre-eruptive magma composition is that volatile species exsolve and are lost from the melt as it ascends and is erupted to the surface. Inclusions of melt trapped within crystals offer a means of measuring pre-eruptive volatile contents, melt evolution, and magma storage depths (Blundy & Cashman, 2005; Moore, 2008; Wallace, 2005).

Owing to abundant rhyolite erupted during the last 25 ka and ongoing unrest signaling that reservoir growth is underway in the upper crust, the Laguna del Maule (LdM) volcanic field is a premier natural laboratory for investigations that seek to link petrologic observations from lava and tephra to the processes that propel surface deformation and seismicity (Andersen et al., 2017, 2019; Singer, Andersen, et al., 2014). U-Th and $^{40}Ar/^{39}Ar$ chronology, mineral-scale diffusion chronology, radiogenic isotopes, and thermodynamic modeling have been applied to LdM to understand rhyolite genesis, storage, and extraction in the shallow crust (Andersen et al., 2017, 2018, 2019; Fierstein, 2018; Hildreth et al., 2010). Moreover, observations from surface-wave seismic tomography, electrical resistivity, gravity, geomorphology, geodesy, and teleseismic tomography reveal a restless modern upper crustal magma reservoir of at least 450 km^3 that is likely mostly frozen but that may host smaller melt-rich domains (Bai et al., 2020; Cordell et al., 2018; Feigl et al., 2013; Le Mével et al., 2015, 2016; Miller et al., 2017; Singer et al., 2018; Wespestad et al., 2019). Taken together, this collection of findings provides a robust framework in which to interpret modern and prehistoric unrest at Laguna del Maule.
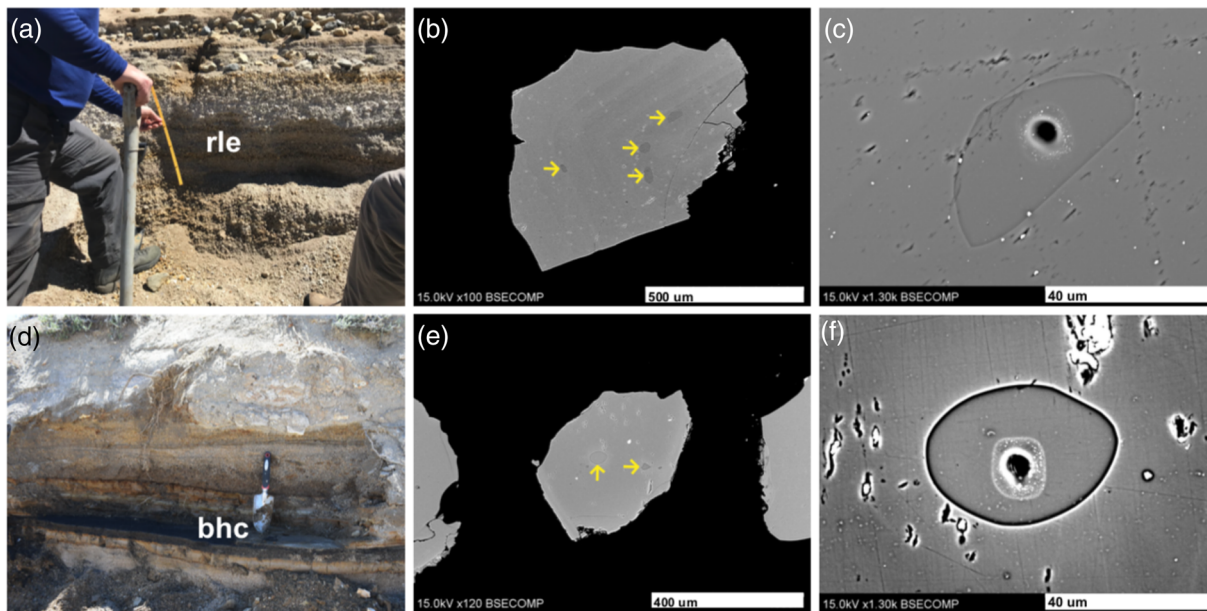
To provide further petrologic leverage with which to interpret the geophysical models and understand the dynamics necessary to repeatedly form and erupt crystal-poor rhyolites in the shallow crust, we present new melt inclusion volatile (H_2O, CO_2, S, F, and Cl) and trace element abundances from LdM rhyolites and basaltic andesite. Results indicate that rhyolitic melts are volatile-rich and that they ascend from 14 to 4 km depth; crystal growth traps melt that reflects progressive fractional crystallization. An exsolved fluid phase likely plays an essential role in the ascent of rhyolite, the depth at which it accumulates, and likelihood of its eruption. Olivine-hosted melt inclusions in basaltic andesite support the hypothesis that rhyolite genesis, pressurization, and eruption triggering are driven by fluids derived from mafic recharge.

2. Geologic and Geophysical Background

The Laguna del Maule volcanic field, in the Andean Southern Volcanic Zone (SVZ), straddles the range crest at 36°S (Figure 1) at elevations between ~2,000 and 3,200 m.a.s.l. Since the last glacial retreat began between

Figure 2. Simplified geologic map, showing the distribution of postglacial lava flows and vents (black stars) within the Laguna del Maule lake basin. Flows outlined in blue were erupted in the early post glacial period (EPG), flows outlined in red were erupted in the Holocene, while flows outlined in black erupted in the interim. Lava flows associated with eruptions included in this study are darker red. Tephra sample locations are indicated by green dots. The vent for bhc is not shown but is located ~14 km west of the lake (Hildreth et al., 2010). Map was modified from Hildreth et al. (2010) and Andersen et al. (2019).

23 and 19 ka, a flare-up of ~40 km^3 of volcanism at LdM has featured predominantly crystal-poor rhyolites, with less frequent rhyodacites, andesites, and basalts (Andersen et al., 2017; Hildreth et al., 2010; Singer, Andersen, et al., 2014). During postglacial time, there have been two episodes of increased rhyolitic volcanism—an early postglacial (EPG) period (from 22.5 to 19 ka) and a Holocene (8.0–1.8 ka) phase, with rhyolitic volcanism concentrated to the southeast of the lake throughout the interim between the EPG and Holocene (Andersen et al., 2018). During the EPG and Holocene, both explosive and effusive rhyolites originated from vents surrounding the LdM lake basin (Figure 2), with the exception of the first eruption, the Rhyolite of Laguna del Maule (rdm), which likely came from a vent currently beneath the northern portion of the modern-day lake (Fierstein, 2018). The 20 km^3 plinian eruption of rdm comprises the only postglacial rhyolite that contains a mafic component (Fierstein, 2018). The mafic component occurs as discrete scoria clasts within the larger rhyolitic fall deposit, although it is a small portion (<1%) of the total volume. The eruption of postglacial andesites and rhyodacites mainly outside of the ring of rhyolite vents encircling the lake is hypothesized to indicate the presence of a sizeable silicic reservoir beneath LdM that interacts with ascending mafic magmas (Hildreth et al., 2010). An abundance of mafic inclusions in each of the rhyodacites, coupled with the lack of quenched mafic inclusions and lack of mineral zoning in rhyolite phenocrysts, as well as uniform whole-rock chemistry of the rhyolites, supports this hypothesis (Andersen et al., 2018; Hildreth et al., 2010).

Recent geochronologic, petrologic, geophysical, and geomorphic studies further support the hypothesis of a large, shallow silicic reservoir residing beneath LdM and indicate that the modern system is exceptionally restless, with ongoing inflation at >25 cm/year since 2007 (Andersen et al., 2017, 2018, 2019; Cordell et al., 2018; Feigl et al., 2013; Le Mével et al., 2016; Miller et al., 2017; Miller, Le Mével, et al., 2017; Singer, Andersen, et al., 2014; Singer et al., 2018; Wespestad et al., 2019). Surface-wave seismic tomography shows a low-shear-wave velocity (V_s) anomaly that corresponds to a >450-km^3 crystal-rich (~5% melt) reservoir at 2 to 8 km depth beneath the northwest portion of the lake at LdM (Wespestad et al., 2019). However, results from magnetotelluric and Bouguer gravity surveys suggest that regions containing a higher concentration of melt may exist within the larger crystal-rich reservoir (Cordell et al., 2018; Miller, Le Mével, et al., 2017). Cordell et al. (2018) suggested that in addition to a shallow conductive region interpreted as partial melt (which they call C3), magnetotelluric surveys also reveal an interconnected, deeper C4 conductor dipping to the north of the lake. A partially molten reservoir in this location may provide heat, volatiles, and melt to the shallow reservoir. A regional scale magnetotelluric study revealed a deep crustal conductor connected to the shallow magma reservoirs beneath LdM and Tatara-San Pedro Volcano (Cordell et al., 2019), consistent with a trans-crustal magma system (Cashman et al., 2017). Seismic tomography results show a major upper crustal low velocity anomaly directly beneath the lake extending to a depth of 12 km that corresponds to an average melt fraction of 14% and melt volume of ~70 km^3 (Bai et al., 2020). Similar to Cordell et al. (2019), seismic tomography shows a middle to deep crustal anomaly to the north and west of LdM, providing more evidence for a trans-crustal magma system feeding volcanism at LdM. Further, the depth, location, and northeast-southwest orientation of the low V_s anomaly is consistent with the 115-km^3 low-density body detected by Miller, Le Mével, et al. (2017) and the location of the ongoing episode of extraordinary surface deformation at LdM observed by InSAR and GPS (Feigl et al., 2013; Le Mével et al., 2015). Current uplift is interpreted to be driven by magma emplacement at a rate of ~0.05 km^3/year within an expanding sill at

Figure 3. (a) Sampled tephra layer from the Los Espejos rhyolite (rle). (b) Representative melt inclusion-bearing plagioclase crystal (melt inclusions shown by yellow arrows). (c) Representative rhyolitic melt inclusion with SIMS pit ~7 µm in diameter. (d) Sampled tephra layer (the black layer) from the basalt of Cerro Hoyo Colorado (bhc). (e) Representative melt inclusion bearing olivine phenocryst. (f) Representative mafic melt inclusion with SIMS pit.

about 4.5 km depth (Le Mével et al., 2016). Moreover, >60 m of paleo-shoreline upwarping implies that similar episodes of magma reservoir growth, uplift, and unrest may have occurred throughout the Holocene beneath the southern portion of the lake basin (Singer et al., 2018).

The narrow range of $^{87}Sr/^{86}Sr$ ratios in LdM rhyolites (0.70407–0.70422) argues that they were generated within the upper crust rather than from partial melting of more radiogenic and heterogenous deep crust (Andersen et al., 2017). A shallow origin is further supported by amphibole barometry, plagioclase hygrometry, and modeling of thermodynamic intensive variables using the MELTS algorithm (Andersen et al., 2017, 2018).

Despite consistent rhyolite whole-rock composition, magnetite, plagioclase, and zircon trace element compositions are distinct in EPG and Holocene eruptive products, suggesting both a spatial and thermochemical shift in the generation of rhyolites at LdM (Andersen et al., 2017, 2018). Moreover, zircon crystallization rates and Ti-in-zircon temperatures indicate that hot zones and regions of cold storage may exist contemporaneously within the mush reservoir at LdM (Andersen et al., 2019). Persistent intrusion of recharge magma is hypothesized to fuel volcanism at LdM and incubate the hot zones creating localized mush bodies with extractable interstitial rhyolitic melt, from which caps of crystal-poor rhyolite are accumulated and erupted (Andersen et al., 2019). LdM plagioclase diffusion timescales indicate short rhyolite residence times (decades to centuries) prior to eruption (Andersen et al., 2018). Relevant to the findings presented here, it is hypothesized that volatiles derived from recharge magma percolate through the mush delivering heat, impacting trace element partitioning, and given a sufficient flux, aid in the extraction, accumulation, and generation of overpressure necessary to erupt rhyolites at LdM (Andersen et al., 2018). A lack of visible surface degassing along with the ongoing unrest may also reflect fluid or volatile accumulation and pressurization at depth, signaling that the magma reservoir at LdM is building toward an explosive, potentially voluminous eruption (Andersen et al., 2018).

3. Materials and Methods

Samples were collected from quickly cooled tephra comprising ash to lapilli up to <4 cm diameter in deposits within well-defined stratigraphic sections (Fierstein, 2018) throughout the lake basin (Figure 2). Analyzed samples include the EPG rhyolites of Laguna del Maule (rdm, ~19 ka) and Espejos (rle, 19.0 ± 0.4 ka) (Figure 3) as well as the Holocene Cerro Barrancas Pyroclastic Flow (rcb-py, 11.4 ± 1.1 ka), the Sin Puerto

rhyodacite (rdsp, <3.5 ka), the southern Cari Launa rhyolite (rsl, 3.3 ± 0.5 ka), and the Nieblas rhyolite (rln, <1.8 ka) (Andersen et al., 2017; Fierstein, 2018). Additionally, three mafic tephras were analyzed, ash of the basalt of Hoyo Cerro Colorado (bhc, 10.2–12.4 ka), and two populations of scoria lapilli associated with the rdm eruption (rdm-b, black scoria and rdm-g, gray scoria that is richer in amphibole). Melt inclusions were measured in the Cerro Barrancas pyroclastic flow (rcb-py) because it formed from a voluminous rhyolitic dome collapse and is the largest single eruptive deposit in the Barrancas complex (Sruoga, 2015). However, most melt inclusions in rcb-py contain bubbles that likely formed due to slow cooling and volatile exsolution within the dome. Thus, estimates of H_2O and CO_2 contents from these inclusions are likely well below those of the actual volatile contents of rhyolite melts from deeper magma sources.

Crystals of plagioclase, quartz, and olivine containing melt inclusions were separated and polished to enable measurement of major and trace element (P, Rb, Sr, Ba, La, Ce, Yb, and Th) and volatile (H_2O, CO_2, S, F, and Cl) composition by electron probe microanalysis (EPMA) and secondary ion mass spectrometry (SIMS). Measured inclusions were glassy, free of crystals and bubbles, lack obvious ruptures, and are thus assumed to be accurate indicators of melt composition at the time of entrapment. Melt inclusion major element-oxide compositions were subsequently measured by wavelength dispersive spectrometry electron probe microanalysis (EPMA) using a CAMECA SXFive field-emission electron probe at UW-Madison. When possible, multiple spots were measured adjacent to the SIMS pit within each melt inclusion. Melt inclusion composition was determined by taking an average of the EPMA spots measured for each inclusion.

For SIMS volatile analyses, the calibration between measured $^{12}C^+$ and CO_2 and measured $^{16}O^1H^+$ and H_2O were determined using rhyolitic and basaltic glasses with known CO_2 and H_2O concentrations (0–1.12 wt. % CO_2 and 0–5.13 wt. % H_2O) (Brooker et al., 1999; Lowenstern & Pitcher, 2013; Mangan & Sisson, 2000) (supporting information Table S2). The H_2O wt. % calibration is based on linear regression of $^{16}O^1H^+/^{28}Si^+$ and $H_2O\%/SiO_2\%$ (Figure S1). The CO_2 calibration is based on linear regression of $^{12}C^+$ intensity normalized to primary-beam intensity (as cps/nA) versus CO_2 ppm (Figure S2). SIMS analyses were carried out using an O^- beam focused to a diameter of 7 μm (Figure 3) at 1.6 nA. The preparation of crystals and EPMA and SIMS methods are further documented in Text S1.

4. Results

A total of 109 melt inclusions hosted in plagioclase, quartz, and olivine were analyzed for major and trace elements and volatiles (Table S1). Aside from nine quartz-hosted inclusions in the rhyolite of Laguna del Maule (rdm), melt inclusions measured in the rhyolitic and rhyodacitic tephras are hosted in plagioclase.

4.1. Melt Inclusion Major Element Compositions

Melt inclusions from the five rhyolitic tephras range in composition from 65.9 to 78.2 wt. % SiO_2; the Holocene rhyodacite (rdsp) contains inclusions with 64.6–71.3 wt. % SiO_2; and melt inclusions hosted in olivine from mafic eruptive products range from 49.4 to 66.9 wt. % SiO_2 (Figure 4). Melt inclusion compositions from rhyolitic and rhyodacitic tephras display a liquid line of descent that is consistent with existing whole-rock data (Andersen et al., 2017; Hildreth et al., 2010) for postglacial silicic volcanism at LdM. Plagioclase- and quartz-hosted inclusions are subtly lower in wt. % CaO, wt. % Al_2O_3, and wt. % FeO* than whole-rock compositions. Olivine-hosted inclusions display more scatter in their MgO, FeO, and Na_2O contents and a less coherent trend when compared to the whole-rock data. Implications of post-entrapment modification and differences between melt inclusion compositions and whole-rock data are discussed further in section 4.4. Rdm-g melt inclusions from the mafic scoria component of the rdm eruption contain a population of more evolved inclusions with significantly lower CaO, MgO, FeO*, and higher SiO_2 (60–67 wt. %) than other olivine-hosted inclusions (49–54 wt. %) (Figure 4). The composition of these olivine-hosted rdm-g inclusions approaches that of some of the least-evolved melt inclusions hosted in plagioclase from the rhyolitic tephra (rdm) from the same eruption.

4.2. Melt Inclusion Trace Element Compositions

Plagioclase-hosted melt inclusions from rhyolitic and rhyodacitic tephras are slightly more enriched in Rb, La, and Ce than the bulk-tephra compositions, consistent with melts that have experienced crystal-liquid fractionation prior to entrapment (Figure 5). Plagioclase-hosted melt inclusions also exhibit lower Sr
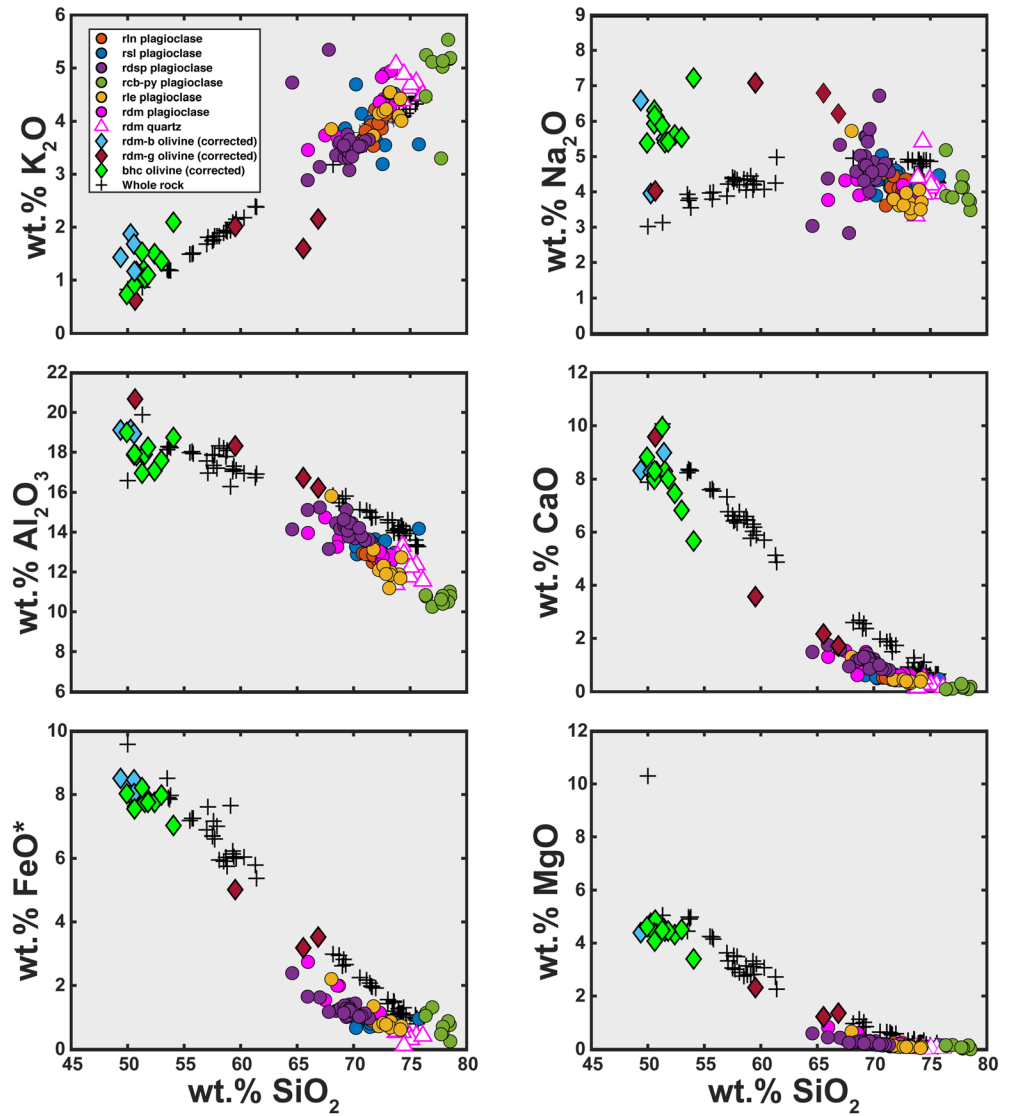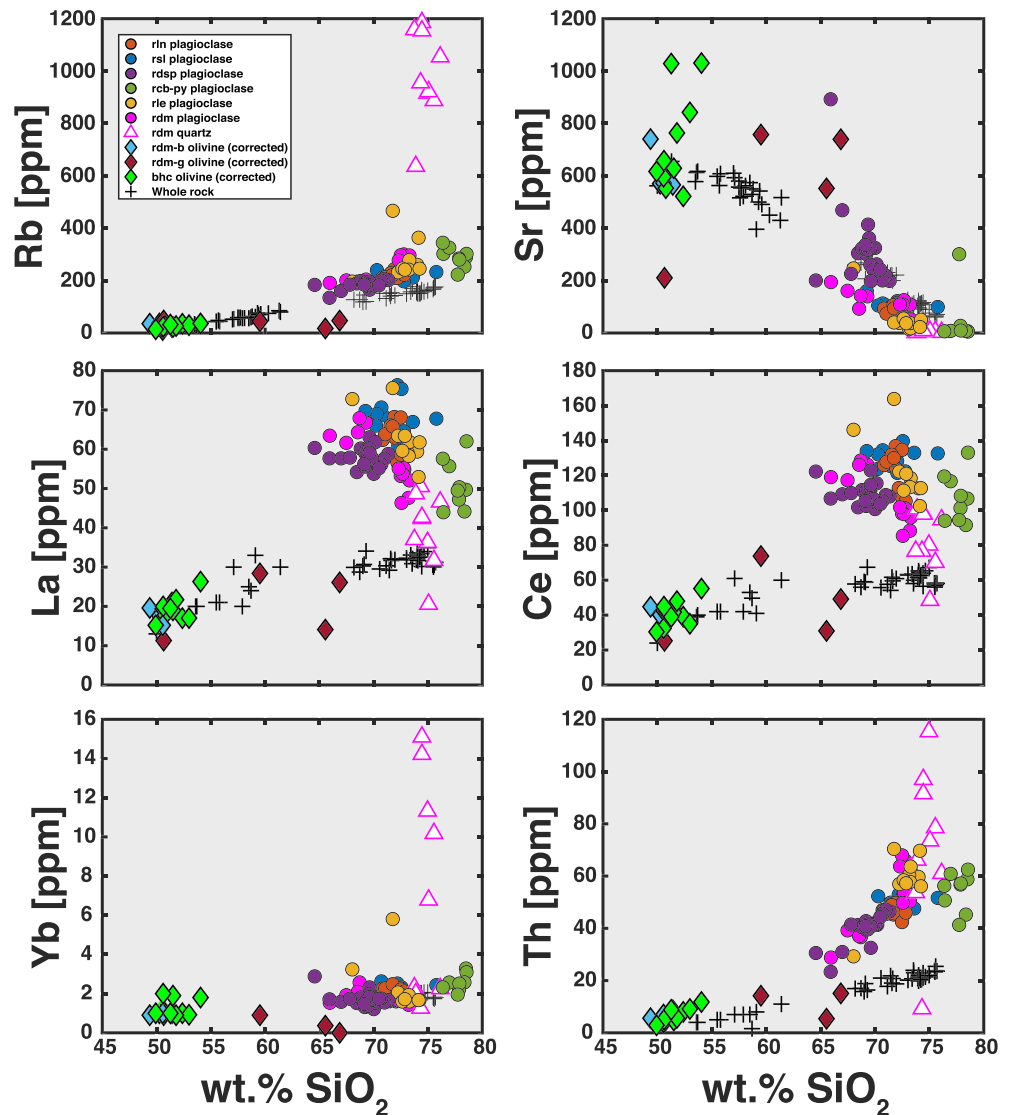
Figure 4. Major element composition of melt inclusions. Olivine compositions are corrected using Danyushevsky and Plechov (2011). Whole-rock data are from Andersen et al. (2017) and Hildreth et al. (2010). Melt inclusion compositions are plotted including volatiles in the total weight percent.

concentrations in comparison to bulk-tephra, consistent with trapping of melt following crystallization of plagioclase from the bulk-magma. EPG rhyolites (rdm and rle) show generally lower values of Ce and La and more elevated concentrations of Th than Holocene rhyolites (rln and rsl). Quartz-hosted melt inclusions from the rdm eruption are significantly more evolved than plagioclase-hosted inclusions from the same eruption. For example, Th, Rb, and Yb concentrations are ~4 to 6 times greater in quartz-hosted inclusions (Figure 5).

4.3. Volatile Composition

The postglacial eruptive products are rich in both H_2O and CO_2. Melt inclusions from rhyolites contain 2.7–7.6 wt. % H_2O, with an average of 5.6 wt. %, and 0–570 ppm CO_2 with an average of 150 ppm (Figure 6). On average quartz-hosted melt inclusions contain roughly equivalent CO_2 and less H_2O than plagioclase-hosted inclusions, 4.6 wt. % versus 5.6 wt. %, respectively. Inclusions from the rhyodacite of Sin Puerto (rdsp) contain 3.7–8.0 wt. % H_2O with an average of 5.8 wt. % and 6–245 ppm CO_2 with an average concentration of 93 ppm. The average water concentrations of both the rhyodacitic and rhyolitic inclusions are consistent

Figure 5. Selected trace element compositions of melt inclusions. Precision of trace element abundances are ~10% (1 SD) (see Table S2).

with estimates from plagioclase-glass hygrometry (Andersen et al., 2018); however, a subset of inclusions from the rhyodacite of Sin Puerto (rdsp) and the rhyolite of Laguna del Maule (rdm) have higher H_2O contents than estimated from plagioclase hygrometry.

Olivine-hosted melt inclusions contain 0–2.5 wt. % H_2O and 0–1,140 ppm CO_2 (Figure 6). The volatile contents measured here are on the lower end of similar inclusions from arc basalts which typically contain ~2–6 wt. % H_2O and up to 2,500 ppm CO_2 (Wallace, 2005). The most H_2O and CO_2 rich inclusions come from the bhc tephra, where the inclusions with the highest water content also contain the highest CO_2 concentrations. The more silicic inclusions from rdm-g scoria also are generally more water-rich than inclusions from the co-erupted rdm-b scoria. However, despite lower H_2O contents the rdm-b melt inclusions contain roughly the same or greater amounts of CO_2 (Figure 6). Melt inclusion data from the SVZ are sparse; however, olivine-hosted melt inclusions from Volcán Llaima (38.7°S) contain 0 to 4.0 wt. % H_2O and 0–1973 ppm CO_2 (Bouvet de Maisonneuve et al., 2012; Ruth et al., 2016). The concentrations of F, S, and Cl of melt inclusions measured in this study are considered to be semi-quantitative values (supporting information) that are useful mainly for delineating relative contrasts between LdM rhyolites.
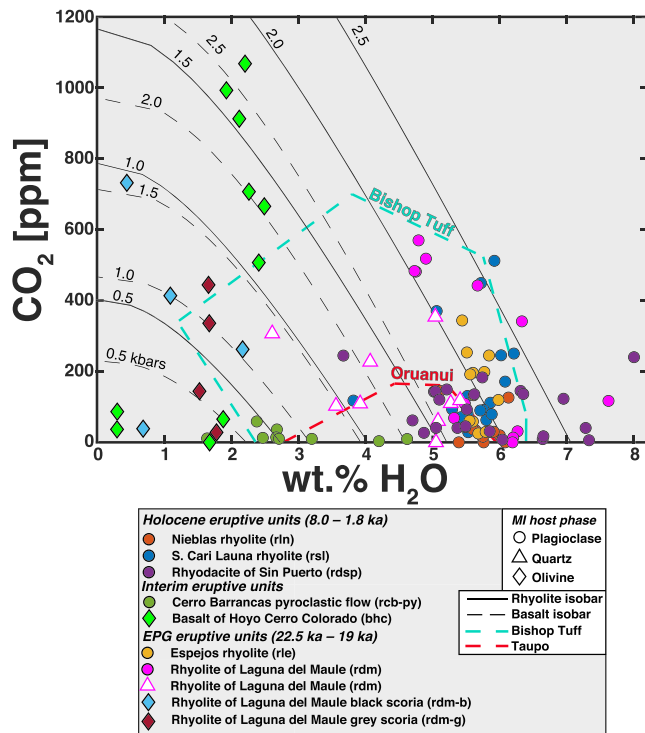
Figure 6. H_2O and CO_2 contents of melt inclusions at Laguna del Maule. Rhyolitic (solid line) and basaltic (dashed line) isobars (kbar) calculated at 800°C (based on thermometry from Andersen et al., 2017) and 1100°C, respectively (Newman & Lowenstern, 2002). The red and turquoise dashed lines show the range in volatile contents reported for the Oruanui eruption from the Taupo Volcanic Zone and the Bishop Tuff, respectively (Liu et al., 2006; Roberge et al., 2013). The precision of H_2O and CO_2 measurements is better than 5% (1 SD) (see Table S2).

4.4. Post-Entrapment Modification Processes

Melt inclusions can be modified by post-entrapment processes such as crystallization, formation of vapor bubbles, and diffusion of elements in or out of the melt inclusion (Danyushevsky et al., 2002; Gaetani et al., 2012; Moore et al., 2015; Steele-Macinnis et al., 2011). These processes can alter the original trapped-melt composition and thus must be considered when interpreting melt inclusion data. The only analyzed inclusions in this study showing textural evidence of modification are in the rhyolitic Cerro Barrancas pyroclastic flow (rcb-py) as they contain bubbles to which a substantial portion of the CO_2 was likely lost (e.g., Moore et al., 2015). Thus, calculated entrapment pressures from these inclusions represent minimum estimates. For all other eruptions studied here melt inclusions containing exsolution or obvious crystallization were avoided for analysis. Pre- and post-analysis all inclusions were carefully screened (via SEM and optical microscopy) for evidence of post-entrapment modification. Any melt inclusions analyzed by SIMS showing evidence of crystallization, ruptures, or bubbles were excluded from interpretation (reasons for exclusion are listed in red at the bottom of Table S2).

Evidence of post-entrapment crystallization (PEC) is not always obvious; thin-rims of crystallized olivine and plagioclase can form at the boundary between melt inclusion and host-phase. Olivine and plagioclase PEC were modeled to assess implications for melt inclusion major and volatile-element concentrations (Figures S7 and S8).

The uncorrected major element composition of olivine-hosted melt inclusions shows evidence of post-entrapment modification when compared to the whole-rock data. The uncorrected data (Table S1) show significant scatter in terms of FeO* and MgO which are both depleted relative to the whole-rock data. Lower MgO contents could be explained by PEC and subsequent re-equilibration of a thin-rim of olivine formed around the edge of the melt inclusion (Danyushevsky et al., 2000, 2002). Diffusion of Fe^+ out of the inclusion can also be accompanied by gain or loss of H^+ (Danyushevsky et al., 2002; Gaetani et al., 2012). To address these factors olivine-hosted melt inclusions were corrected for major element, trace element, and water contents using Petrolog3 (Danyushevsky & Plechov, 2011). Resulting melt inclusion compositions reflect a liquid line of descent that is much more consistent with the whole-rock data (Figure 4).

PEC was also modeled for plagioclase-hosted inclusions. However, the uncorrected melt inclusion data from plagioclase- and quartz-hosted inclusions are used for discussion going forward. Unlike olivine-hosted inclusions, the uncorrected data follow a reasonable liquid line of descent and melt inclusions lack textural evidence of crystallization. Plagioclase-hosted inclusions that are subtly lower in wt. % CaO, wt. % Al_2O_3, and wt. % FeO* than whole-rock data may reflect an artifact of comparing melt inclusion results to bulk-rock data as opposed to more evolved matrix-glass compositions. However, the effect of 1%, 5%, 10%, and 20% PEC in silicic melt inclusions was modeled by adding plagioclase back into the melt using a method similar to Neave et al. (2017). The implications for different degrees of plagioclase PEC are shown in Figures S6 and S7. If 10% PEC is considered it would result in a ~0.5 wt. % drop in H_2O concentrations which translates to ~0.25 kbar drop in the calculated entrapment pressures.

5. Discussion

5.1. Melt Inclusion Entrapment Pressures

Assuming that melts are volatile saturated, the mixed solubility relationship between H_2O and CO_2 can be used to calculate a pressure of entrapment from melt inclusion volatile contents. The solubility model of Newman and Lowenstern (2002) was used to calculate entrapment pressures (Figure 7). Calculations for
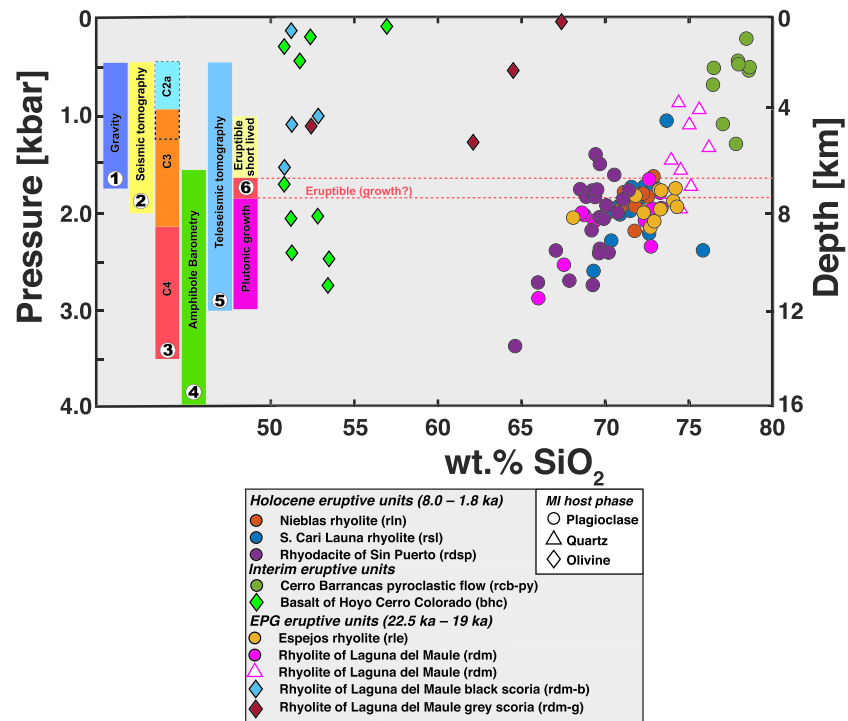
Figure 7. Plot of pressure versus melt inclusion SiO_2 content. Colored bars in the left side of the panel represent depth ranges of rhyolite storage and crystallization inferred from: (1) Bouguer gravity (Miller, Le Mével, et al., 2017), (2) seismic tomography (Wespestad et al., 2019), (3) magnetotellurics (C3 and C4 are conductive regions containing partial melt; C2a is a less conductive region that may contain a low fraction of partial melt [Figure 7]; Cordell et al., 2018), (4) amphibole barometry (Andersen et al., 2017), (5) teleseismic tomography (Bai et al., 2020), and (6) an analytical model that accounts for competing timescales of magma cooling, thermal relaxation of the surrounding crust, and rate of magma recharge. This model suggests optimal depths for silicic magma reservoir growth, storage, and eruptibility as shown (Huber et al., 2019).

plagioclase- and quartz-hosted inclusions were carried out using Fe-Ti oxide temperatures from Andersen et al. (2017). Entrapment pressures and isobars for olivine-hosted inclusions were calculated assuming a temperature of 1100°C (based on MELTS calculations). Depth estimates were calculated assuming lithostatic pressure, with crustal densities of 2,400 kg/m³ from 0 to 4 km depth and 2,600 kg/m³ deeper than 4 km (Figure 7).

Entrapment pressures derived from melt inclusion compositions help constrain pre-eruptive magma storage conditions. However, it is important to remember that melt inclusions provide data on conditions at the time of entrapment, not necessarily those immediately preceding eruption. Quartz and plagioclase-hosted melt inclusions from rhyolitic tephras were trapped at pressures ranging from 0.9 to 3.0 kbar, corresponding to depths of ~4–12 km (Figure 7); 83% of these inclusions were trapped at pressures less than 2.2 kbar with an average of 2.1 kbar. Notably, the quartz-hosted melt inclusions from the rdm eruption contain less water and are restricted to a lower pressure (0.9–2.0 kbar) and temperature storage regime. Thus, plagioclase likely saturated at higher pressure and crystallized earlier than quartz. Progressive plagioclase crystallization drove the melt composition toward higher SiO_2, incompatible trace elements (Figure 5), and lower CaO and Al_2O_3 (Figure 4) as the melt decompressed and cooled. Together, plagioclase- and quartz-hosted inclusions provide a near continuous record of primarily decompression-driven fractional crystallization, and H_2O exsolution, as the rdm magma ascended from the mid-crust into shallower portions of the LdM magma reservoir (Figure 7).

An alternative explanation is that the quartz-hosted melt inclusions in the rdm eruption represent melt trapped during near-solidus crystallization in the long-lived crystal mush beneath LdM. This could explain the extreme enrichment of these melt inclusions in Rb, Th, and Yb and lower water concentrations (2.6–5.4 wt. % H_2O). In this case lower H_2O contents would result from diffusion out of the inclusion due to

protracted storage at elevated temperatures (Zajacz et al., 2009). Thus, the quartz-hosted inclusions may represent material that was remobilized or "unthawed" from the crystal mush prior to eruption (Andersen et al., 2017; Cooper & Kent, 2014; Rubin et al., 2017). Rdm was the largest of the postglacial eruptions at LdM and thus may have been more capable of remobilizing near-solidus material; this could explain why similar melt inclusions are not observed in other eruptions. However, one issue with this interpretation is that the elevated CO_2 concentrations (up to 350 ppm) observed in the quartz-hosted melt inclusions would not be expected in near-solidus crystallization of rhyolite.

Inclusions from the rhyodacite of Sin Puerto (rdsp) were trapped deeper at pressures of 1.6 to 3.5 kbar, corresponding to a depth range of 6.5–14.0 km. The average entrapment pressure from rdsp inclusions is 2.2 kbar; however, one third of the inclusions were trapped at pressures greater than 2.5 kbar. The less silicic rdsp melt inclusions were trapped at pressures greater than nearly all melt inclusions from the rhyolites (Figure 7). This is consistent with crystallization of volatile saturated dacitic to rhyodacitic crystal-rich mush underlying the domain where most rhyolite is stored (Andersen et al., 2017; Hildreth et al., 2010). Volatile compositions from olivine-hosted melt inclusions give comparable entrapment pressures to the rhyolites and rhyodacites, with pressures ranging from 0.1 to 2.7 kbar corresponding to depths of ~0 to 11 km (Figure 7). However, none of the olivine-hosted melt inclusions record higher pressures than the highest-pressure melt inclusions from the rhyodacite. Since H^+ can diffuse and re-equilibrate rapidly in olivine (Gaetani et al., 2012) it is possible that the volatile load delivered to the base of the mush could potentially be larger (or smaller) than the 2.5 wt. % H_2O and 1,040 ppm CO_2 concentrations recorded in olivine-hosted melt inclusions. Despite this, the high pressure most volatile-rich olivine-hosted inclusions are a useful proxy for the recharge melt intruding into the base of the dacitic mush underlying LdM. Here the mafic recharge likely stalls, as it cools and begins to crystallize, H_2O and CO_2 exsolve and ascend into the overlying mush (Andersen et al., 2018).

5.2. Role of Volatiles at LdM

Rhyolites and rhyodacites at LdM exhibit high H_2O and CO_2 concentrations. Melt inclusions in typical arc rhyolites contain between 4 and 6 wt. % H_2O (Wallace et al., 2015). A subset of inclusions from the LdM rhyolites and rhyodacites analyzed here contain >7 wt. % H_2O. For comparison, rhyolitic melt inclusions from the Bishop Tuff and the Oruanui eruption from Taupo Volcanic Zone contain from 1.2 to 6.3 wt. % H_2O and 6 to 699 ppm CO_2 (Roberge et al., 2013) and 2.8–6.0 wt. % H_2O and <160 ppm CO_2 (Liu et al., 2006), respectively (Figure 6).

No discernable shift in the overall volatile contents is observed between EPG and Holocene rhyolites at LdM (Figure S4). The average water contents of melt inclusions from each individual EPG and Holocene rhyolite are all between 5 and 6 wt. % H_2O, suggesting that the volatile content of silicic magmas at LdM has remained relatively constant during the last ~25 ka. The exception is the Cerro Barrancas pyroclastic flow (rcb-py), which was deposited in the interim between the EPG and Holocene episodes of activity (Andersen et al., 2017). It formed a block and ash deposit via a rhyolitic dome collapse (Sruoga, 2015) and contains notably lower volatile contents (<4.6 wt. % H_2O and <60 ppm CO_2) (Figure S4). The trapped rcb-py melt also contains elevated SiO_2, K_2O, and incompatible trace elements (Figures 4 and 5), reflecting extensive shallow fractional crystallization of the dome-forming magma prior to collapse.

Although H_2O and CO_2 contents of melt inclusions in EPG and Holocene rhyolites are broadly similar (Figure S4), there are ranges of volatile contents within individual eruptions (Figure 6). For example, the southern Cari Launa rhyolite (rsl) exhibits H_2O and CO_2 concentrations ranging from 3.8–6.2 wt. % and 70–510 ppm, respectively. Wide ranges in H_2O and CO_2 concentrations in individual eruptions can be attributed to variable effects of ascent, crystallization, and CO_2 fluxing (Blundy & Cashman, 2005; Caricchi et al., 2018; Newman & Lowenstern, 2002). In many of the analyzed tephras, the fact that CO_2 is more variable than H_2O can be attributed to the preferential exsolution of CO_2 due to a sharp drop in CO_2 solubility with the ascent of volatile saturated magma, coupled with the release of CO_2-rich fluid as crystallization proceeds (Blundy & Cashman, 2008; Caricchi et al., 2018; Ghiorso & Gualda, 2015; Newman & Lowenstern, 2002). The variation in H_2O and CO_2 (Figure 6) in LdM rhyolites can be explained mainly by a combination of decompression and CO_2 flushing.
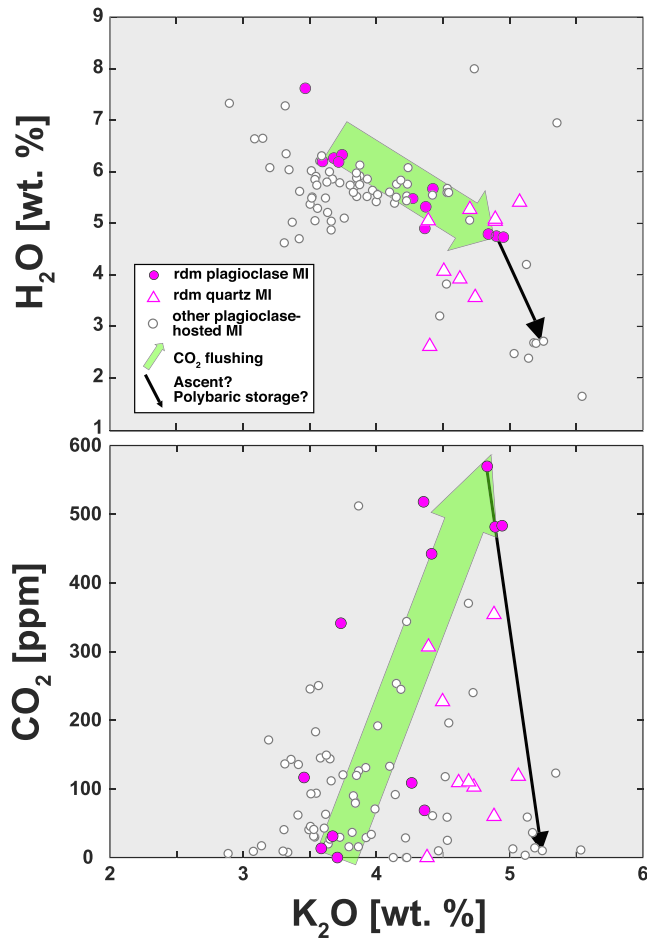
Figure 8. H_2O and CO_2 versus K_2O variation diagrams. The top plot shows general trend of decreasing H_2O with increasing K_2O in LdM which can be explained by ascent and crystallization assuming K_2O behaves incompatibly (Blundy & Cashman, 2008). However, the population of melt inclusions exhibiting high CO_2, high K_2O, and low H_2O concentrations is best explained by CO_2 flushing (Caricchi et al., 2018). In both diagrams the green arrow schematically illustrates the effect of CO_2 flushing, whereas the black arrow illustrates the effects of decompression or polybaric storage. Evidence of CO_2 flushing is most clearly expressed by inclusions in the rdm tephra (pink circles and triangles).

Intrusion of mafic recharge magma at LdM is hypothesized to repeatedly deliver exsolved volatiles to the overlying mush at LdM (Andersen et al., 2018; Hildreth et al., 2010). H_2O likely comprises most of the delivered fluid phase; however, the addition of even a small amount of exsolved CO_2 can have important implications for silicic reservoirs. Repeated flushing of CO_2-rich fluids into H_2O-saturated magma will impart chemical changes that may be recorded by melt inclusions. Increasing the partial pressure of CO_2 in the fluid phase leads to progressive dissolution of CO_2 into the silicic melt and causes concomitant exsolution of H_2O (Caricchi et al., 2018; Ghiorso & Gualda, 2015; Newman & Lowenstern, 2002). Exsolution of H_2O will promote crystallization via the associated increase in liquidus temperature. Thus, when compared to other melt inclusions from the same eruption, melt inclusions with lower concentrations of H_2O, elevated CO_2, and elevated K_2O (or other incompatibly behaving element) are best explained by CO_2 flushing (Caricchi et al., 2018). CO_2 flushing is most evident in the melt inclusions from the 20 km^3 EPG rdm eruption (Figure 8). Plagioclase- and quartz-hosted inclusions from this eruption show high K_2O, moderate to high CO_2 concentrations, and lower H_2O. A few of the rdm plagioclase-hosted inclusions show higher water and low CO_2 suggesting that these may have been trapped prior to the presence of an exsolved CO_2-rich fluid. Melt inclusions in Espejos rhyolite (rle) and Cari Launa rhyolite (rsl) appear to also reflect trends consistent with CO_2 flushing; however, the evidence is less clear (Figure 8). This suggests that CO_2 flushing was more impactful in generating rhyolites connected to the deeper plumbing at LdM. However, evidence of CO_2 flushing in the other tephras could also be obscured by simultaneous effects of crystallization and decompression.

CO_2 flushing is consistent with the recharge-driven processes hypothesized to fuel the formation of rhyolites at LdM (Andersen et al., 2018; Hildreth et al., 2010). An increasingly abundant exsolved-volatile phase would lower bulk-magma density and explain the Bouguer gravity low beneath LdM (Miller, Le Mével, et al., 2017). Increasing magma volume and decreasing magma density due to an increasingly abundant exsolved-volatile phase has been suggested as a mechanism to generate overpressures that can destabilize a magma reservoir (e.g., Biggs & Pritchard, 2017; Caricchi et al., 2014). Caricchi et al. (2018) model CO_2 flushing of silicic magmas under a variety of conditions including injection of 0.01–10 wt. % CO_2 at pressures ranging from 1.0 to 3.0 kbar. Simulations show that the addition of sufficient exsolved CO_2 to a reservoir with eruptible magma (<50% crystallinity) is a plausible eruption trigger. These models demonstrate that the rate of pressure increase is maximized when only 0.1 wt. % fluid CO_2 is added to a reservoir at 1.0 kbar (~4 to 5 km depth), in other words conditions remarkably consistent with those of LdM. Although LdM melt inclusions generally record pressures higher than 1.0 kbar, the eruptible upper portion of this reservoir likely extends to depths of 4 km (Figure 7), and the CO_2 load delivered via mafic recharge is up to 1,100 ppm or ~0.1 wt. % (based on olivine-hosted melt inclusion analyses). The total amount of CO_2 that might flush the shallow silicic reservoir reflects not only the CO_2 concentration in the olivine-hosted melt inclusion, but the mass of the recharge magma added relative to rhyodacitic and rhyolitic magma. Given the volatile contents of olivine-hosted melt inclusions, and the pervasive abundance of quenched mafic inclusions in the rhyodacitic lavas (Andersen et al., 2017; Hildreth et al., 2010), we suggest that rapid CO_2 flushing is a plausible eruption-triggering mechanism at LdM.
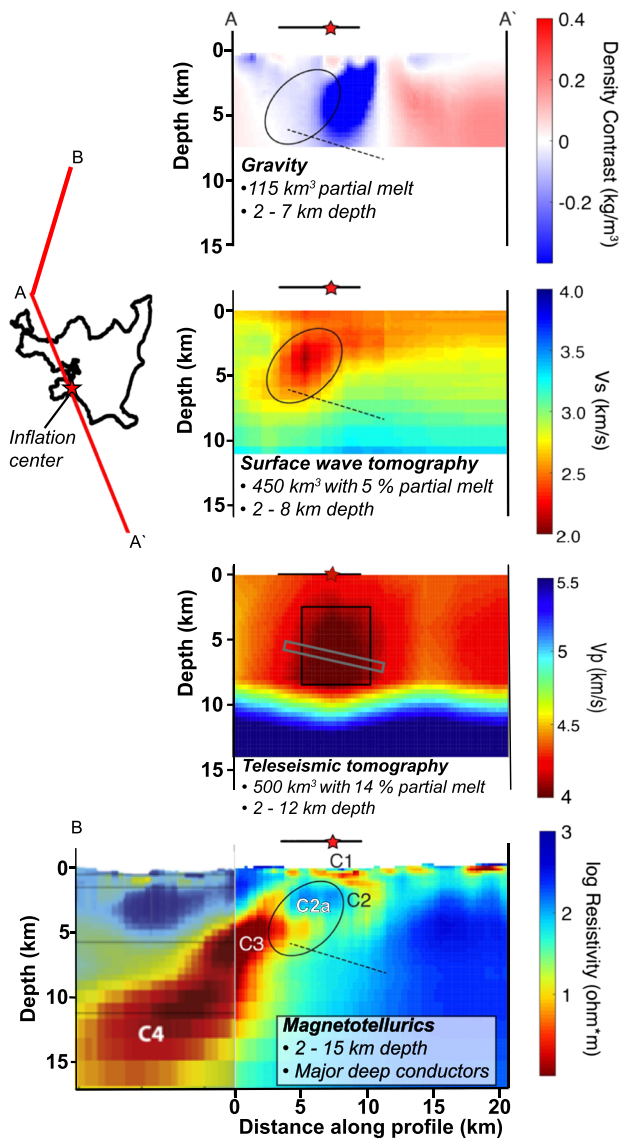
Figure 9. Cross-sectional comparison of gravity (Miller, Le Mével, et al., 2017), surface-wave seismic tomography (Wespestad et al., 2019), teleseismic tomography (Bai et al., 2020), and electrical resistivity/magnetotellurics (Cordell et al., 2018) at LdM. In the lowermost panel, the moderately conductive domain C2a is inferred to contain a small percentage of water undersaturated rhyolite melt that is co-located with the low V_s domain in the surface wave seismic tomography model of the second panel from the top (Wespestad et al., 2019). The inclined dashed line shows position of inflating sill modeled to drive current surface inflation (Feigl et al., 2013; Le Mével et al., 2015).

5.3. Integration of Melt Inclusion Data With Geophysical and Petrologic Observations

Constraining magmatic storage conditions is essential to understanding the dynamics and evolution of magma reservoirs. The major and trace element and H_2O, CO_2, Cl, and F contents of LdM melt inclusions provide new insight on the depths of magma storage, melt segregation, and crystallization processes, as well as links between mafic and silicic components in the LdM system. Here we integrate the melt inclusion findings with those from seismic, magnetotellurics, gravity, geodesy, and petrochronology to build a more comprehensive appreciation of what propels the generation and eruption of LdM rhyolites (Figure 9). It is important to note that storage conditions indicated by melt inclusion entrapment pressures and thermobarometry need not mirror modern geophysical observations. The location and extent of melt present in the reservoir have almost certainly evolved from 20 ka to present.

Amphibole barometry (Andersen et al., 2017) yields pressures (1.7–4.0 kbar) that are consistent with the vast majority of melt inclusion entrapment pressures (Figure 7). Further, melt inclusion entrapment pressures record crystallization consistent with magma storage near the base of and slightly deeper than, the modern, 450 km³ reservoir identified by seismic tomography at 2–8 km beneath LdM (Wespestad et al., 2019) (Figures 7 and 9). However, there is a smaller subset of inclusions that records mid-crustal crystallization, extending as deep as ~12 km in the rhyolites and ~14 km in the rhyodacite. These less-evolved, more volatile-rich melts were likely trapped deeply within the trans-crustal magma system thought to underlie LdM (Andersen et al., 2017; Cordell et al., 2019). The surface-wave tomography approach used by Wespestad et al. (2019) is unable to resolve contrasts in V_s deeper than ~11 km. Thus, the low V_s reservoir imaged by seismic tomography and low-density domain detected by gravity may represent only the upper region of the mostly frozen reservoir beneath the lake basin.

Using magnetotelluric (MT) data, Cordell et al. (2018) interpreted two deeper conductors to reflect the presence fluid or melt (Figure 9). One (C3) is located at depths of 4 to 8 km beneath the northern portion of the LdM basin and overlaps with the low V_s domain imaged seismically (Wespestad et al., 2019). The other (C4) connects to the C3 conductor, dips northward away from the LdM basin, and extends to depths of >15 km (Cordell et al., 2018). The C3 conductor has low bulk resistivity indicating a magma body that contains >4 wt. % H_2O dissolved in the melt. Wespestad et al. (2019) reinterpreted the MT data to show that small fractions of melt with modest dissolved H_2O (consistent with that of seismic results) may

exist in a domain of moderate conductivity between the C2 and C3 conductors at depths of 2 to 5 km (C2a in Figure 9). Melt inclusions containing high concentrations of H_2O and CO_2 in rdm and its basaltic to andesitic inclusions are consistent with cooling, crystallization, and differentiation of magmas initiating at depths corresponding to the C4 conductor and also within the C3 and C2a domains (Figures 7 and 9). Thus, the upper 15 km of the northern LdM magma plumbing system may be little altered from its configuration during the EPG phase of rhyolite production (Figure 10) (Cordell et al., 2018; Wespestad et al., 2019).

Teleseismic tomography indicates a major low velocity anomaly with a volume of ~500 km³ located directly beneath the lake at LdM at depths of 2 to 12 km (Bai et al., 2020). Average P-velocities suggest an average
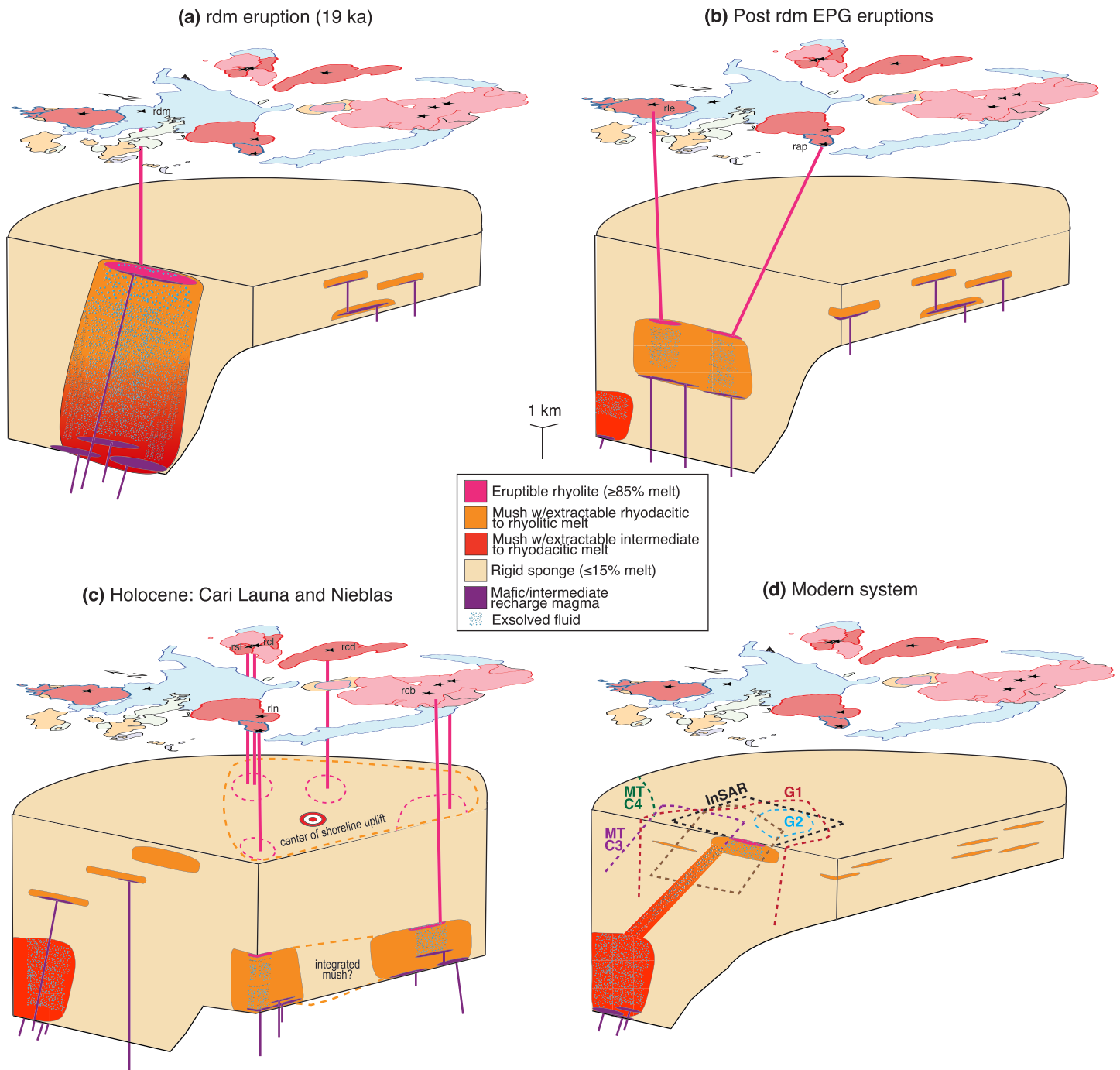
Figure 10. Conceptual cartoon of the evolution of postglacial volcanism at LdM (modified from Andersen et al., 2019). (a) The 20 km³ rhyolite of Laguna del Maule (rdm) was extracted from a well-connected middle to shallow crustal mush reservoir. The eruption also included a volumetrically minor co-erupted mafic component. (b) The Espejos (rle) and Arroyo Palacios (rap; no analyzed melt inclusions) units are the last two EPG rhyolites and appear to not have been extracted from the deeper mid-crustal plumbing. (c) Holocene magma intrusion shifted southward (Singer et al., 2018). Similar to the rle eruption, melt inclusions from Nieblas rhyolite (rln) do not display evidence of a deeper plumbing system. However, high pressure, volatile-rich inclusions from Cari Launa rhyolite (rsl) suggest melt extraction from deeper regions of the reservoir was re-established further north in the basin at LdM (although not visible in the cartoon above). (d) Hypothesized current state of the LdM system based on petrologic and geophysical studies.

melt fraction of 14% corresponding to a total melt volume of ~70 km³. The spatial extent of the anomaly is consistent with the shallow crustal reservoir observed via surface-wave tomography (Figure 9; Wespestad et al., 2019) and gravity (Miller, Le Mével, et al., 2017). Consistent with magnetotellurics and melt

inclusion entrapment pressures (Figure 7), teleseismic tomography results indicate regions of partial melt exist at depths of 12 km or deeper (Bai et al., 2020). Deeper low velocity anomalies are likely concealed by shallower ones of similar size (Bai et al., 2020); thus melt extraction from deeper than 12 km (similar to melt inclusions found in the rhyodacite) is plausible. Similar to Cordell et al. (2019), teleseismic results show that melt exists at lower crustal depths supporting the presence of a trans-crustal magma system fueling volcanism.

Las Nieblas (rln) represents the most recent eruption of rhyolite within the LdM basin (Hildreth et al., 2010). The modern center of inflation and low V_s domain imaged seismically are located only a few kilometers from its vent (Figure 2) (Wespestad et al., 2019). Although only 10 plagioclase-hosted melt inclusions from the Nieblas eruption were analyzed, entrapment pressures record a narrow range of storage conditions consistent with crystallization at depths of ~7–9 km (Figure 7). Unlike most of the other analyzed rhyolitic and rhyodacitic tephras, rln does not contain a sub-population of inclusions with entrapment pressures corresponding to depths of greater than 10 km. This suggests that the Nieblas rhyolite may have been extracted from an isolated portion of the shallow silicic, crystal-rich reservoir that has grown vertically and laterally during the last 20 ka and is thus now less well-connected to the deeper portions of the system to the north (Figure 10).

The shallow silicic magma reservoir underlying the LdM basin from which rhyolite has been repeatedly extracted may be fueled by melt and volatiles derived from andesitic to rhyodacitic magmas extending to depths of >15 km north of the LdM basin. This hotter, deeper portion of the magmatic system likely experiences repeated input of basaltic recharge magma, differentiation of magmas toward rhyodacitic compositions, build-up of both H_2O and CO_2 that help propel magma ascent, further crystallization, extraction of rhyolitic melt, and perhaps second boiling that may promote inflation and eruption from the shallow portion of the system.

The ongoing and Holocene surface deformation at Laguna del Maule may reflect the emplacement of mafic magma into the base of an extensive silicic reservoir at depths of 7–4 km (Andersen et al., 2017, 2018; Le Mével et al., 2016; Singer et al., 2018). However, melt inclusion compositions presented here indicate that rhyolitic melt is present in some parts of the system at deeper levels than previously thought. Thus, rhyolitic magma, ascending from depths of ~12 km may, in parallel with ascending mafic recharge magma, drive reservoir growth and surface inflation. The widespread presence of rhyolitic magma at depths of 12 to 7 km that intercepts ascending mafic magmas may also explain the lack of co-erupted mafic material in all but the rdm rhyolite (Andersen, Jicha, et al., 2017; Hildreth et al., 2010). The rdm eruption may reflect an unusual flux of mafic magma that mobilized ascent of copious rhyolitic melt from the deepest levels of the mostly frozen magma reservoir (Figure 10).

As discussed above, an exsolved volatile phase likely plays a key role in the incubation, formation, and eruption of rhyolites at LdM. Using MELTS simulations Andersen et al. (2018) show that external fluxing of volatiles sourced from mafic recharge is necessary to produce the low densities inferred from the Bouguer gravity model of Miller, Le Mével, et al. (2017). Measured volatile contents of the olivine-hosted melt inclusions in this study can be used as a proxy for the dissolved volatile load of the basaltic andesite recharge into the base of the mush beneath LdM. MELTS calculations suggest that basaltic andesite melt inclusions in olivine with 2.5 wt. % H_2O and 1,140 ppm CO_2 would have a density of 2,450 kg/m^3 at 2.0 kbar. One km^3 of such melt contains 6.1×10^{10} kg of H_2O and 2.8×10^9 kg CO_2. Based on a H_2O fluid density of 420 kg/m^3 for H2O and 590 kg/m^3 for CO_2 at 800°C (Span & Wagner, 1996), 1 km^3 of recharge melt could deliver 0.15 km^3 of exsolved H_2O and 0.005 km^3 of CO_2. Despite the relatively small volume of CO_2, flushing of the reservoir with CO_2 encourages exsolution of H_2O, further enhancing fluid accumulation (Collins et al., 2009). Modeling of geodetically measured inflation at LdM suggests that influx of new melt at 0.025 to 0.050 km^3/year into a sill at ~5 km depth can drive the ongoing deformation (Le Mével et al., 2016). At these rates of intrusion, 0.08 km^3 of exsolved H_2O could accumulate in 10 years of magma recharge, delivered at rates consistent with ongoing unrest at LdM. Thus, delivery of recharge magma with ~2.5 wt. % H_2O and 1,100 ppm CO_2 on timescales of decades may readily supply fluid in excess of that required to drive the observed inflation and act as a triggering mechanism for a typical LdM eruption of <3 km^3 (Andersen et al., 2018). Moreover, shallow crystal-poor magma reservoirs require injection of only modest amounts of CO_2 (~1,000 ppm) to generate the necessary overpressure for eruption relative to deeper crystal-rich

reservoirs (Caricchi et al., 2018). Hence, we infer that modest CO_2 flushing and accumulation of exsolved fluid, in part derived from repeated mafic recharge, may lead to eruptions at LdM.

Despite nearly homogenous whole-rock compositions, trace element compositions in melt inclusions from LdM rhyolites display evidence of shifting magmatic conditions and discrete magma batches associated with EPG and Holocene eruptions (Figure 10). To illustrate the contrasting pre-eruptive thermochemical conditions with time, Andersen et al. (2018) highlighted lower Ce contents in plagioclase from EPG rhyolites than in the Holocene. We observe the same pattern in EPG and Holocene melt inclusion Ce contents (Figure S8). Halogens have been shown to decrease the partitioning of rare-earth elements into crystallizing phases by increasing rare-earth sites in the melt (Andersen et al., 2018; Ponader & Brown, 1989). At LdM, generally lower Cl contents in EPG rhyolites correlate to lower Ce contents in melt inclusions and the reverse in Holocene rhyolites (Figure S8). Thus, it appears that higher Cl contents in Holocene melts may have inhibited/reduced Ce partitioning into crystallizing plagioclase. However, there is no clear correlation between melt F and Ce contents. Nevertheless, the distinct Ce and Cl contents observed in EPG and Holocene melt inclusions support the evolution of discrete domains of eruptible rhyolite with time.

Quartz is present above trace levels only in the rdm tephra. Quartz-hosted inclusions in rdm record higher SiO_2 and incompatible trace element concentrations than plagioclase-hosted inclusions from the same eruption (Figures 4 and 5). This suggests that the melt in the quartz-hosted inclusions was trapped following fractional crystallization of melt similar to that trapped in the plagioclase. Moreover, the volatile contents (Figure 6) and resulting entrapment pressures (Figure 7) of quartz-hosted inclusions are lower than those of the plagioclase-hosted inclusions, indicating that they formed at shallower depths. Based on Yb/Gd ratios in zircon, Andersen et al. (2019) propose a thermal gradient with cooler, titanite-saturated melt in the upper portion of the rdm reservoir. Thus, quartz likely saturated and began crystalizing at lower temperatures and pressures as the magma ascended through the reservoir. Taken together, plagioclase- and quartz-hosted melt inclusions record nearly continuous differentiation (from dacite to rhyolite) and melt extraction from mush spanning from 12–14 to 4 km depth (Figures 7 and 10). In support of this hypothesis, MELTS modeling of decompression-driven crystallization of rhyodacite magma reproduces melt inclusion compositional variation (Figure S9). Thus, CO_2 flushing-induced and ascent-driven crystallization of silicic melts originating from mush in the mid-crust is a viable mechanism for generating rhyolites at LdM.

An alternative possibility is that crystal growth and trapping of melt inclusions occurs throughout the depth range where silicic mush is stored, leading to elevated H_2O contents in the melt inclusions trapped at higher pressure (Figure 7). An interpretation along these lines is consistent with models which suggest that ascent-driven decompression promotes only minor crystallization, making it unlikely inclusions recording continuous melt evolution will be trapped (Caricchi et al., 2018). However, results from diffusion chronology in plagioclase (Andersen et al., 2018) indicate that rhyolite exists only ephemerally (decades to centuries) at LdM. Disequilibrium trace element profiles preserved ubiquitously in plagioclase indicate that there is little lag time between plagioclase growth, ascent, and eruption. Thus, although polybaric storage and crystallization may be important, the repeated, rapid extraction, and eruption of rhyolite from the mush also highlights an important role for rhyolite production via decompression-driven fractional crystallization (Andersen et al., 2018).

An analytical model that integrates competing timescales of magma cooling, thermal relaxation of the surrounding crust, and rate of magma recharge suggests optimal depths for silicic magma reservoir growth, storage, and eruptibility (Huber et al., 2019). The array of depths recorded by melt inclusion entrapment pressures agrees well with the modeled optimal pressure range (1.5 to 2.5 kbar) required to grow and erupt silicic magmas in the Huber et al. (2019) model (Figure 7). This model suggests that reservoir expansion at shallow depth is strongly encouraged by the presence of an exsolved volatile phase and rapid recharge rates, which both feature prominently at LdM. Storage of erupted LdM rhyolites in this optimal depth window is, however, very brief, as plagioclase diffusion chronometry indicates decade to century intervals separating periods of near equilibrium crystallization, from disequilibrium crystal growth, ascent, and eruption (Andersen et al., 2018) that reflect the decompression recorded by melt inclusions (Figure 7).

5.4. Summary of Magma Reservoir Evolution at LdM

Figure 10 shows a conceptual cartoon of the evolution of postglacial volcanism at LdM (modified from Andersen et al., 2019). The rhyolite of Laguna del Maule (rdm) was the largest (20 km^3) of the postglacial eruptions at LdM. Melt inclusions from this eruption record less-evolved (dacitic), more volatile-rich melts that were extracted from deeper within the mush (red regions in Figure 10) than following eruptions. Melt extraction was likely aided by an excess volatile phase derived from ascent-driven exsolution, CO_2 flushing, and possibly second boiling. Accumulation of excess volatiles may also have played a key role in eruption triggering. Fractional crystallization drove melt from dacitic to rhyolitic compositions (Figure S9; orange and pink regions in Figure 10) as it cooled and ascended into the shallow crust prior to eruption. The eruption also included a volumetrically minor co-erupted mafic component (purple regions in Figure 10). The Espejos (rle) and Palacios (rap; no analyzed melt inclusions) units represent the last two rhyolites erupted from the EPG mush. Inclusions from the Espejos eruption were not trapped deeper than 10 km. This implies that the mush which produced the rle eruption was less well-connected to the deeper mid-crustal plumbing. During the Holocene, the shallow magma reservoir expanded southward (Singer et al., 2018). Similar to the rle eruption, melt inclusions from Nieblas rhyolite (rln) do not display evidence of a deeper plumbing system. However, high pressure, volatile-rich inclusions from Cari Launa rhyolite (rsl) suggest melts extracted from deeper regions of the reservoir were able to erupt in this northeastern corner of the LdM basin. Modern geophysical observations are consistent with the petrology (Andersen et al., 2017, 2018) of postglacial eruptions and suggest that a shallow, potentially eruptible, body of rhyolitic melt currently exists within the larger reservoir beneath LdM (Cordell et al., 2018; Feigl et al., 2013; Le Mével et al., 2016, 2015; Miller, Le Mével, et al., 2017; Wespestad et al., 2019). Based on the consistency of depth ranges between high pressure melt inclusions and the modern C4 conductor observed via magnetotellurics (Cordell et al., 2018), we hypothesize a deeper mush to the northwest of LdM, in which volatile-rich rhyodacitic to rhyolitic melt resides and feeds the shallower, more southerly reaches of the reservoir (Figure 10).

6. Conclusions

Petrologic, geochronologic, and geophysical evidence yield complementary perspectives on magmatic processes and storage conditions beneath LdM. Postglacial rhyolites at LdM are H_2O and CO_2 rich, and although their volatile concentrations remained steady, distinct trace element abundances of EPG and Holocene melt inclusions reveal that discrete magma batches were generated and erupted over the last 20 ka. Melt inclusion compositions and entrapment pressures reveal that rhyolitic magma ascends from ~14–8 km depth as it differentiates, exsolves H_2O, and accumulates in the shallow crust (~8–4 km) as crystal-poor, buoyant melt. Mafic recharge into the deeper reaches of the mostly frozen silicic magma reservoir likely incubates and expands the reservoir in addition to flushing it with a substantial volume of both H_2O and CO_2. Extraction of silicic melt is aided by an abundant exsolved volatile phase sourced from ascent-driven exsolution, second boiling, and mafic recharge magma. The accumulation of an exsolved fluid phase at LdM could potentially generate sufficient overpressure to trigger eruption. In this context, the ongoing inflation, coupled with no clear observations of pressure release via fumaroles or surface degassing, may be warning signs that the LdM system is building toward an explosive eruption.

Data Availability Statement

Data supporting our conclusions can be accessed via Dryad (https://datadryad.org/stash/share/LIfz2ayofpXXBgk-sEInDFtNS0kCPMaFR0bB_n_sGPw).

References

Andersen, N. L., Jicha, B. R., Singer, B. S., & Hildreth, W. (2017). Incremental heating of Bishop Tuff sanidine reveals preeruptive radiogenic Ar and rapid remobilization from cold storage. *Proceedings of the National Academy of Sciences*, *114*(47), 12,407–12,412. https://doi.org/10.1073/pnas.1709581114

Andersen, N. L., Singer, B. S., & Coble, M. A. (2019). Repeated rhyolite eruption from heterogeneous hot zones embedded within a cool, shallow magma reservoir. *Journal of Geophysical Research: Solid Earth*, *124*, 1–19. https://doi.org/10.1029/2018JB016418

Andersen, N. L., Singer, B. S., Costa, F., Fournelle, J., Herrin, J. S., & Fabbro, G. N. (2018). Petrochronologic perspective on rhyolite volcano unrest at Laguna del Maule, Chile. *Earth and Planetary Science Letters*, *493*, 57–70. https://doi.org/10.1016/j.epsl.2018.03.043

Andersen, N. L., Singer, B. S., Jicha, B. R., Beard, B. L., Johnson, C. M., & Licciardi, J. M. (2017). Pleistocene to Holocene growth of a large upper crustal rhyolitic magma reservoir beneath the active Laguna del Maule Volcanic Field, Central Chile. *Journal of Petrology*, *58*(1), 85–114. https://doi.org/10.1093/petrology/egx006

Annen, C., Blundy, J. D., & Sparks, R. S. J. (2006). The genesis of intermediate and silicic magmas in deep crustal hot zones. *Journal of Petrology*, *47*(3), 505–539. https://doi.org/10.1093/petrology/egi084

Bachmann, O., & Bergantz, G. W. (2004). On the origin of crystal-poor rhyolites: Extracted from batholithic crystal mushes. *Journal of Petrology*, *45*(8), 1565–1582. https://doi.org/10.1093/petrology/egh019

Bachmann, O., & Bergantz, G. W. (2006). Gas percolation in upper-crustal silicic crystal mushes as a mechanism for upward heat advection and rejuvenation of near-solidus magma bodies. *Journal of Volcanology and Geothermal Research*, *149*(1–2), 85–102. https://doi.org/10.1016/j.jvolgeores.2005.06.002

Bai, T., Thurber, C., Lanza, F., Singer, B. S., & Keranen, K. (2020). Teleseismic tomography of the Laguna del Maule Volcanic Field in Chile. *Journal of Geophysical Research*, *125*, e2020JB019449. https://doi.org/10.1029/2020JB019449

Barboni, M., Boehnke, P., Schmitt, A. K., Harrison, T. M., Shane, P., Bouvier, A.-S., & Baumgartner, L. (2016). Warm storage for arc magmas. *Proceedings of the National Academy of Sciences*, *113*(49), 13,959–13,964. https://doi.org/10.1073/pnas.1616129113

Biggs, J., & Pritchard, M. E. (2017). Global volcano monitoring: What does it mean when volcanoes deform? *Elements*, *13*(1), 17–22. https://doi.org/10.2113/gselements.13.1.17

Blundy, J., & Cashman, K. (2005). Rapid decompression-driven crystallization recorded by melt inclusions from Mount St. Helens volcano. *Geology*, *33*(10), 793–796. https://doi.org/10.1130/G21668.1

Blundy, J., & Cashman, K. (2008). Petrologic reconstruction of magmatic system variables and processes. *Reviews in Mineralogy and Geochemistry*, *69*(1), 179–239. https://doi.org/10.2138/rmg.2008.69.6

Bouvet de Maisonneuve, C., Dungan, M. A., Bachmann, O., & Burgisser, A. (2012). Insights into shallow magma storage and crystallization at Volcán Llaima (Andean Southern Volcanic Zone, Chile). *Journal of Volcanology and Geothermal Research*, *211–212*, 76–91. https://doi.org/10.1016/j.jvolgeores.2011.09.010

Brooker, R. A., Kohn, S. C., Holloway, J. R., McMillan, P. F., & Carroll, M. R. (1999). Solubility, speciation and dissolution mechanisms for CO_2 in melts on the $NaAlO_2$-SiO_2 join. *Geochimica et Cosmochimica Acta*, *63*(21), 3549–3565. https://doi.org/10.1016/S0016-7037(99)00196-9

Caricchi, L., Annen, C., Blundy, J., Simpson, G., & Pinel, V. (2014). Frequency and magnitude of volcanic eruptions controlled by magma injection and buoyancy. *Nature Geoscience*, *7*(2), 126–130. https://doi.org/10.1038/ngeo2041

Caricchi, L., Sheldrake, T. E., & Blundy, J. (2018). Modulation of magmatic processes by CO_2 flushing. *Earth and Planetary Science Letters*, *491*, 160–171. https://doi.org/10.1016/j.epsl.2018.03.042

Cashman, K. V., Sparks, R. S. J., & Blundy, J. D. (2017). Vertically extensive and unstable magmatic systems: A unified view of igneous processes. *Science*, *355*(6331). https://doi.org/10.1126/science.aag3055

Collins, S. J., Pyle, D. M., & Maclennan, J. (2009). Melt inclusions track pre-eruption storage and dehydration of magmas at Etna. *Geology*, *37*(6), 571–574. https://doi.org/10.1130/g30040a.1

Cooper, K. M., & Kent, A. J. R. (2014). Rapid remobilization of magmatic crystals kept in cold storage. *Nature*, *506*(7489), 480–483. https://doi.org/10.1038/nature12991

Cordell, D., Unsworth, M. J., & Díaz, D. (2018). Imaging the Laguna del Maule Volcanic Field, central Chile using magnetotellurics: Evidence for crustal melt regions laterally-offset from surface vents and lava flows. *Earth and Planetary Science Letters*, *488*, 168–180. https://doi.org/10.1016/j.epsl.2018.01.007

Cordell, D., Unsworth, M. J., Diaz, D., Reyes-Wagner, V., Currie, C. A., & Hicks, S. P. (2019). Fluid and melt pathways in the central Chilean subduction zone near the 2010 Maule earthquake (35–36°S) as inferred from magnetotelluric data. *Geochemistry, Geophysics, Geosystems*, *20*, 1818–1835. https://doi.org/10.1029/2018GC008167

Danyushevsky, L. V., Della-Pasqua, F. N., & Sokolov, S. (2000). Re-equilibration of melt inclusions trapped by magnesian olivine phenocrysts from subduction-related magmas: Petrological implications. *Contributions to Mineralogy and Petrology*, *138*(1), 68–83. https://doi.org/10.1007/PL00007664

Danyushevsky, L. V., McNeill, A. W., & Sobolev, A. V. (2002). Experimental and petrological studies of melt inclusions in phenocrysts from mantle-derived magmas: An overview of techniques, advantages and complications. *Chemical Geology*, *183*(1–4), 5–24. https://doi.org/10.1016/S0009-2541(01)00369-2

Danyushevsky, L. V., & Plechov, P. (2011). Petrolog3: Integrated software for modeling crystallization processes. *Geochemistry, Geophysics, Geosystems*, *12*, 25–45. https://doi.org/10.1029/2011GC003516

Degruyter, W., Huber, C., Bachmann, O., Cooper, K. M., & Kent, A. J. R. (2017). Influence of exsolved volatiles on reheating silicic magmas by recharge and consequences for eruptive style at Volcán Quizapu (Chile). *Geochemistry, Geophysics, Geosystems*, *18*, 4123–4135. https://doi.org/10.1002/2017GC007219

Druitt, T. H., Costa, F., Deloule, E., Dungan, M., & Scaillet, B. (2012). Decadal to monthly timescales of magma transfer and reservoir growth at a caldera volcano. *Nature*, *482*(7383), 77–80. https://doi.org/10.1038/nature10706

Feigl, K. L., Le Mével, H., Tabrez Ali, S., Córdova, L., Andersen, N. L., DeMets, C., & Singer, B. S. (2013). Rapid uplift in Laguna del Maule volcanic field of the Andean southern volcanic zone (Chile) 2007–2012. *Geophysical Journal International*, *196*(2), 885–901. https://doi.org/10.1093/gji/ggt438

Fierstein, J. (2018). Postglacial eruptive history established by mapping and tephra stratigraphy provides perspectives on magmatic system beneath Laguna del Maule, Chile. In *Chapman Conference on Merging Geophysical, Petrochronologic, and Modeling Perspectives of Large Silicic Magma Systems*, Abstract. Quinamavida, Chile.

Gaetani, G. A., O'Leary, J. A., Shimizu, N., Bucholz, C. E., & Newville, M. (2012). Rapid reequilibration of H_2O and oxygen fugacity in olivine-hosted melt inclusions. *Geology*, *40*(10), 915–918. https://doi.org/10.1130/G32992.1

Gelman, S. E., Gutiérrez, F. J., & Bachmann, O. (2013). On the longevity of large upper crustal silicic magma reservoirs. *Geology*, *41*(7), 759–762. https://doi.org/10.1130/G34241.1

Ghiorso, M. S., & Gualda, G. A. R. (2015). An H_2O–CO_2 mixed fluid saturation model compatible with rhyolite-MELTS. *Contributions to Mineralogy and Petrology*, *169*(6), 1–30. https://doi.org/10.1007/s00410-015-1141-8

Hartung, E., Weber, G., & Caricchi, L. (2019). The role of H_2O on the extraction of melt from crystallising magmas. *Earth and Planetary Science Letters*, *508*, 85–96. https://doi.org/10.1016/j.epsl.2018.12.010

Hildreth, W. (2004). Volcanological perspectives on Long Valley, Mammoth Mountain, and Mono Craters: Several contiguous but discrete systems. *Journal of Volcanology and Geothermal Research*, *136*(3–4), 169–198. https://doi.org/10.1016/j.jvolgeores.2004.05.019

Hildreth, W., Godoy, E., Fierstein, J., & Singer, B. S. (2010). Laguna del Maule volcanic field: Eruptive history of a Quaternary basalt to rhyolite distributed volcanic field on the Andean range crest in central Chile. *Servicio Nacional de Geologia y Mineria, Bolletin*, *63*(63), 145.

Huber, C., Bachmann, O., & Dufek, J. (2011). Thermo-mechanical reactivation of locked crystal mushes: Melting-induced internal fracturing and assimilation processes in magmas. *Earth and Planetary Science Letters*, *304*(3–4), 443–454. https://doi.org/10.1016/j.epsl.2011.02.022

Huber, C., & Parmigiani, A. (2018). A physical model for three-phase compaction in silicic magma reservoirs. *Journal of Geophysical Research: Solid Earth*, *123*, 2685–2705. https://doi.org/10.1002/2017JB015224

Huber, C., Townsend, M., Degruyter, W., & Bachmann, O. (2019). Optimal depth of subvolcanic magma chamber growth controlled by volatiles and crust rheology. *Nature Geoscience*, *12*(9), 762–768. https://doi.org/10.1038/s41561-019-0415-6

Jackson, M. D., Blundy, J., & Sparks, R. S. J. (2018). Chemical differentiation, cold storage and remobilization of magma in the Earth's crust. *Nature*, *564*(7736), 405–409. https://doi.org/10.1038/s41586-018-0746-2

Le Mével, H., Feigl, K. L., Cõrdova, L., DeMets, C., & Lundgren, P. (2015). Evolution of unrest at Laguna del Maule volcanic field (Chile) from InSAR and GPS measurements, 2003 to 2014. *Geophysical Research Letters*, *42*, 6590–6598. https://doi.org/10.1002/2015GL064665

Le Mével, H., Gregg, P. M., & Feigl, K. L. (2016). Magma injection into a long-lived reservoir to explain geodetically measured uplift: Application to the 2007–2014 unrest episode at Laguna del Maule volcanic field, Chile. *Journal of Geophysical Research: Solid Earth*, *121*, 6092–6108. https://doi.org/10.1002/2016JB013066

Liu, Y., Anderson, A. T., Wilson, C. J. N., Davis, A. M., & Steele, I. M. (2006). Mixing and differentiation in the Oruanui rhyolitic magma, Taupo, New Zealand: Evidence from volatiles and trace elements in melt inclusions. *Contributions to Mineralogy and Petrology*, *151*(1), 71–87. https://doi.org/10.1007/s00410-005-0046-3

Lowenstern, J. B., & Pitcher, B. W. (2013). Analysis of H_2O in silicate glass using attenuated total reflectance (ATR) micro-FTIR spectroscopy. *American Mineralogist*, *98*(10), 1660–1668. https://doi.org/10.2138/am.2013.4466

Mangan, M., & Sisson, T. (2000). Delayed, disequilibrium degassing in rhyolite magma: Decompression experiments and implications for explosive volcanism. *Earth and Planetary Science Letters*, *183*(3–4), 441–455. https://doi.org/10.1016/S0012-821X(00)00299-5

Miller, C. A., Le Mével, H., Currenti, G., Williams-Jones, G., & Tikoff, B. (2017). Microgravity changes at the Laguna del Maule volcanic field: Magma-induced stress changes facilitate mass addition. *Journal of Geophysical Research: Solid Earth*, *122*, 3179–3196. https://doi.org/10.1002/2017JB014048

Miller, C. A., Williams-Jones, G., Fournier, D., & Witter, J. (2017). 3D gravity inversion and thermodynamic modelling reveal properties of shallow silicic magma reservoir beneath Laguna del Maule, Chile. *Earth and Planetary Science Letters*, *459*, 14–27. https://doi.org/10.1016/j.epsl.2016.11.007

Moore, G. (2008). Interpreting H_2O and CO_2 contents in melt inclusions: Constraints from solubility experiments and modeling. *Reviews in Mineralogy and Geochemistry*, *69*(1), 333–362. https://doi.org/10.2138/rmg.2008.69.9

Moore, L. R., Gazel, E., Tuohy, R., Lloyd, A. S., Esposito, R., Steele-MacInnis, M., et al. (2015). Bubbles matter: An assessment of the contribution of vapor bubbles to melt inclusion volatile budgets. *American Mineralogist*, *100*(4), 806–823. https://doi.org/10.2138/am-2015-5036

Neave, D. A., Hartley, M. E., Maclennan, J., Edmonds, M., & Thordarson, T. (2017). Volatile and light lithophile elements in high-anorthite plagioclase-hosted melt inclusions from Iceland. *Geochimica et Cosmochimica Acta*, *205*, 100–118. https://doi.org/10.1016/j.gca.2017.02.009

Newman, S., & Lowenstern, J. B. (2002). Volatile Calc: A silicate melt–H_2O–CO_2 solution model written in visual basic for excel. *Computational Geosciences*, *28*, 597–604. https://doi.org/10.1016/S0098-3004(01)00081-4

Parmigiani, A., Faroughi, S., Huber, C., Bachmann, O., & Su, Y. (2016). Bubble accumulation and its role in the evolution of magma reservoirs in the upper crust. *Nature*, *532*(7600), 492–495. https://doi.org/10.1038/nature17401

Ponader, C. W., & Brown, G. E. (1989). Rare earth elements in silicate glass melt systems: II. Interactions of La, Gd, and Yb with halogens. *Geochimica et Cosmochimica Acta*, *53*(11), 2905–2914. https://doi.org/10.1016/0016-7037(89)90167-1

Pritchard, M. E., Mather, T. A., McNutt, S. R., Delgado, F. J., & Reath, K. (2019). Thoughts on the criteria to determine the origin of volcanic unrest as magmatic or non-magmatic. *Philosophical Transactions of the Royal Society A: Mathematical, Physical and Engineering Sciences*, *377*(2139), 20180008. https://doi.org/10.1098/rsta.2018.0008

Reath, K., Pritchard, M., Biggs, J., Andrews, B., Ebmeier, S. K., Bagnardi, M., et al. (2020). Using conceptual models to relate multiparameter satellite data to subsurface volcanic processes in Latin America. *Geochemistry, Geophysics, Geosystems*, *21*, e2019GC008494. https://doi.org/10.1029/2019GC008494

Roberge, J., Wallace, P. J., & Kent, A. J. R. (2013). Magmatic processes in the Bishop Tuff rhyolitic magma based on trace elements in melt inclusions and pumice matrix glass. *Contributions to Mineralogy and Petrology*, *165*(2), 237–257. https://doi.org/10.1007/s00410-012-0807-8

Rubin, A. E., Cooper, K. M., Till, C. B., Kent, A. J. R., Costa, F., Bose, M., et al. (2017). Rapid cooling and cold storage in a silicic magma reservoir recorded in individual crystals. *Science*, *356*, 1154–1156. https://doi.org/10.1126/science.aam8720

Ruth, D. C. S., Cottrell, E., Cortés, J. A., Kelley, K. A., & Calder, E. S. (2016). From passive degassing to violent Strombolian eruption: The case of the 2008 eruption of Llaima volcano, Chile. *Journal of Petrology*, *57*(9), 1833–1864. https://doi.org/10.1093/petrology/egw063

Singer, B. S., Andersen, N. L., Le Mével, H., Feigl, K. L., DeMets, C., Tikoff, B., et al. (2014). Dynamics of a large, restless, rhyolitic magma system at Laguna del Maule, southern Andes, Chile. *GSA Today*, *24*, 4–10. https://doi.org/10.1130/GSATG216A.1

Singer, B. S., Costa, F., Herrin, J. S., Hildreth, W., & Fierstein, J. (2016). The timing of compositionally-zoned magma reservoirs and mafic 'priming' weeks before the 1912 Novarupta-Katmai rhyolite eruption. *Earth and Planetary Science Letters*, *451*, 125–137. https://doi.org/10.1016/j.epsl.2016.07.015

Singer, B. S., Jicha, B. R., Fournelle, J. H., Beard, B. L., Johnson, C. M., Smith, K. E., et al. (2014). Lying in wait: Deep and shallow evolution of dacite beneath Volcán de Santa María, Guatemala. *Geological Society, London, Special Publications*, *385*(1), 209–234. https://doi.org/10.1144/SP385.2

Singer, B. S., Le Mével, H., Licciardi, J. M., Córdova, L., Tikoff, B., Garibaldi, N., et al. (2018). Geomorphic expression of rapid Holocene silicic magma reservoir growth beneath Laguna del Maule, Chile. *Science Advances*, *4*(6), eaat1513. https://doi.org/10.1126/sciadv.aat1513

Span, R., & Wagner, W. (1996). A new equation of state for carbon dioxide covering the fluid region from the triple-point temperature to 1100 K at pressures up to 800 MPa. *Journal of Physical and Chemical Reference Data*, *25*(6), 1509–1596. https://doi.org/10.1063/1.555991

Sruoga, P. (2015). Actividad explosiva postglacial del centro barrancas, complejo volcanico Laguna del Maule (36° 05′ S, 70° 30′ O). In *Congreso Geologico Chileno* (pp. 49–52). La Serena, Chile: Sociedad Geológica de Chile.

Steele-macinnis, M., Esposito, R., & Bodnar, R. J. (2011). Thermodynamic model for the effect of post-entrapment crystallization on the H_2O-CO_2 systematics of vapor-saturated, silicate melt inclusions. *Journal of Petrology*, *52*(12), 2461–2482. https://doi.org/10.1093/petrology/egr052

Till, C. B., Vazquez, J. A., & Boyce, J. W. (2015). Months between rejuvenation and volcanic eruption at Yellowstone caldera, Wyoming. *Geology*, *43*(8), 695–698. https://doi.org/10.1130/G36862.1

Wallace, P. J. (2005). Volatiles in subduction zone magmas: Concentrations and fluxes based on melt inclusion and volcanic gas data. *Journal of Volcanology and Geothermal Research*, *140*(1–3), 217–240. https://doi.org/10.1016/j.jvolgeores.2004.07.023

Wallace, P. J., Plank, T., Edmonds, M., & Hauri, E. H. (2015). Volatiles in magmas. *The Encyclopedia of Volcanoes*, *Second Edition*, 163–183. https://doi.org/10.1016/b978-0-12-385938-9.00007-9

Wark, D. A., Hildreth, W., Spear, F. S., Cherniak, D. J., & Watson, E. B. (2007). Pre-eruption recharge of the Bishop magma system. *Geology*, *35*(3), 235–238. https://doi.org/10.1130/G23316A.1

Wespestad, C. E., Thurber, C. H., Andersen, N. L., Singer, B. S., Cardona, C., Zeng, X., et al. (2019). Magma reservoir below Laguna del Maule volcanic field, Chile imaged with surface-wave tomography. *Journal of Geophysical Research: Solid Earth*, *124*, 2858–2872. https://doi.org/10.1029/2018JB016485

Zajacz, Z., Hanley, J. J., Heinrich, C. A., Halter, W. E., & Guillong, M. (2009). Diffusive reequilibration of quartz-hosted silicate melt and fluid inclusions: Are all metal concentrations unmodified? *Geochimica et Cosmochimica Acta*, *73*(10), 3013–3027. https://doi.org/10.1016/j.gca.2009.02.023

Reference From the Supporting Information

Jochum, K. P., Stoll, B., Herwig, K., Willbold, M., Hofmann, A. W., Amini, M., et al. (2006). MPI-DING reference glasses for in situ microanalysis: New reference values for element concentrations and isotope ratios. *Geochemistry, Geophysics, Geosystems*, *7*, Q02008. https://doi.org/10.1029/2005GC001060